Analysis and real-time prediction of the full-scale thrust for floating wind turbine based on artificial intelligence

Xue Jiang[1], Sandy Day[1], David Clelland[1], Xu Liang[2]

[1]Department of naval architecture, ocean and marine engineering, University of Strathclyde, G15AE, UK

[2]Ocean College, Zhejiang University, Ocean Engineering Building, Zhoushan Campus, Zhejiang University, Dinghai, Zhoushan, 316021, China

Abstract: In this paper, numerous aero-hydro-servo-elastic coupled simulations are carried out in time-domain to observe the performance of the real-time thrust acting on the rotor of the OC3-Hywind offshore floating wind turbine. And the studying focuses on investigating the correlation between inputs (surge motion, pitch motion, wind conditions, etc.) and the targeted output (rotor thrust) in the time domain. Besides, artificial intelligence (AI) techniques are used to estimate a prediction model of real-time thrust based on the data from simulations. To predict the thrust, data for four comparative coupled environmental conditions are considered, by which the effect of turbulence and wave spectrum on the thrust force is also investigated. Moreover, a series of simulations of frequency-increasing regular wave conditions and speed-increasing wind conditions are carried out to observe their effect on the real-time rotor thrust. Additionally, the impact of the pitch and surge RAOs of the floating foundation and the wind velocity are quantitatively studied. It reveals that the high-frequency response of thrust is dominated by wave change, whereas low-frequency response is dominated by wind change. Besides, one simulation model of the thrust acting on the rotor is estimated regarding high-frequency and low-frequency response separately to account the dominating influence.

Keywords: Fully-coupled simulation; OC3-Hywind; real-time thrust prediction; Artificial neural network; impact analyses on the real-time thrust

1. Introduction

During recent few years, the development of grid-connected floating wind turbines has flourished. It is claimed that the more into the sea, there is more wind energy, since the increase of wind velocity[1]. It is exciting that we have seen a few social achievements, especially the deployment of the Hywind floating wind farm in Scotland in 2017, which is the first floating wind farm in the world[2]. Indeed, this spar-type floating wind turbine has experienced sufficient research as shown in Fig. 1. [3] deals with the modelling and parameter tuning OC3-Hywind floating wind turbine with a tuned mass damper (TMD) installed in the nacelle. The seakeeping performance of the OC3-Hywind platform is investigated in [4] by both numerical solution and model test method. Moreover, a series of model test researches have been performed at the same time[5-7].

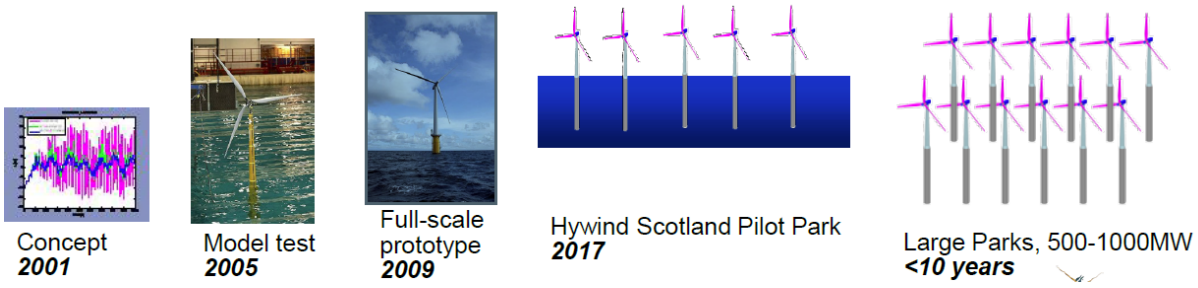

Fig. 1 The development of Hywind Scotland

Different from fixed-bottom wind turbines, the floating platform naturally responds to wave loadings which are Froude-scaled, while the turbine forces react to aerodynamic loads which are Reynolds-scaled. Commonly Froude scaling is used in tank tests. However, using Froude scaling also for the wind turbine rotor will lead to wrong aerodynamic loads compared to the full-scale turbine. It is essential to model the aerodynamic loads for FOWTs correctly. One possible method of shaping a floating wind turbine in the laboratory environment is to employ a working rotor in a wind field generated by a series of fans. Experimental studies with a wind field generated by a set of fans in a tank are usually used to examine the hydrodynamic or

aerodynamic performance of a floating wind model. For example, Martin et al. tried to account for Reynolds effects by appropriate distortion of the rotor geometry[8], however, it is incredibly challenging to construct and operate a working scale rotor due to the large size, not to mention the very lightweight, and sophisticated control requirements, see references[9-12]. Moreover, examples are given by Chujo et al. for a spar OWT in [13], by K Muller et al. for a semi-submersible OWT in [14], and by Goupee et al. for the spar, semi-submersible and TLP types in [15]. The experiments study are usually focused on a scaled model in the region of 1/50 – 1/100. However, both Froude similitude and Reynolds similitude cannot be satisfied simultaneously in the small-scale model tests of ships and offshore structures.

And some common difficulties are concluded, such as lack of wind generation in a hydrodynamic laboratory, issues of simulation of spread moorings, or issues of the similarity between the model and full-scale prototype in [16]. Notably, the simulation of wind loading for tank testing of floating wind turbines presents a variety of severe challenges, particularly challenges concerning the wind generation. Therefore, many people turn to numerical tools, for example, Liu et al.[17] develope a CFD simulation tool for the fully coupled model of floating wind turbines. Godine Kok et al.[18] develope a hydrodynamic computer module to evaluate the linear and nonlinear loads on floating wind turbines using a new fluid-impulse formulation for coupling with the FAST program, for more details see reference[19]. However, physical experiments are still needed, in spite of the difficulty in correctly modelling the aerodynamic loads with the proper hydrodynamic influence taken into account.

A few recent articles review the approaches of simulating wind loading on floating wind turbines in wave tanks. For example, Fowler et al. use a high-speed fan located on the model in line with the rotor drivetrain is to generate the thrust component of the wind load [20]. Bayati et al. proposed a six-degree-of-freedom platform to simulate the motions of the platform of the floating wind turbine[21]. Additionally, the six-degree-of-freedom platform is used to carry

out tests to measure the movements and the aero-dynamic thrust related to the instantaneous position. Moreover, the velocity of the platform is calibrated in real time using a modified version of the FAST aero-hydro-servo-elastic simulation code, which proves it possible to use the thrust calculated from FAST to generate the equivalent thrust in the model test. More before, Chujo et al. attach a lightweight line at the rotor hub and tension[22]. However, that approach can only be justified for rough preliminary estimation of the maximum mooring offset. Kraskowski et al.[23] use a fan rotating at a constant speed in stationary air generating a predefined thrust to represent the mean rotor thrust, which and allows for easy adjustment of the mean wind load and simulation of mean mooring offsets. Therefore, inspired by those researches, the idea of "software in the loop" simulation(SIL) approach is formed.

Motivated by the problems mentioned above and research potentials, the authors aim at proposing a new approach to utilise the idea of "software-in-the-loop" in which we use an active control system inserted with AI model to handle the inputs from experiments and give out a proper thrust command to drive a fan in real time in Fig. 2. By thus to enable the accurate tank test of a floating wind turbine and overcomes the various limitations labs are facing.

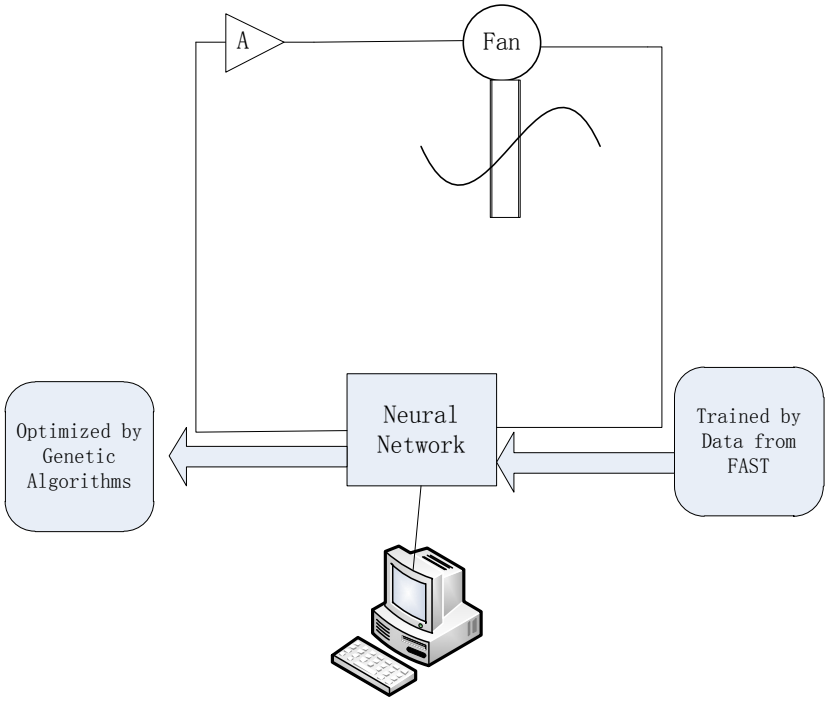

Fig. 2 The diagram of the software-in-the-loop application concept

To simulate or predict actuated forces correctly acting on the model, AI models (simulation model and prediction model) can simulate and predict the rotor thrust in real time with an acceptable degree of accuracy are required. For this purpose, the fully-coupled calculation code of floating wind turbines -FAST is used to run a number of simulations, and the data are thoroughly analysed to obtain a reasonable control structure. A series of simulations of frequency-increasing regular wave conditions and speed-increasing wind conditions are carried out to observe their effect on the real-time rotor thrust. Additionally, the effect of the pitch and surge RAOs of the floating foundation and the wind velocity are quantitatively studied. It reveals that the high-frequency response of thrust is dominated by wave change, whereas low-frequency response is dominated by wind change. Therefore, one simulation model of the thrust acting on the rotor is estimated regarding high-frequency and low-frequency response separately to account the dominating influences. To predict the thrust in more complexed environmental conditions, data for four comparative coupled environmental conditions are considered. They are respectively the irregular wave condition demonstrated by JONSWAP spectrum combined with turbulent wind or the corresponding steady wind, the Pierson-Moskowitz coupled with the same turbulent or steady wind conditions, by which the effect of turbulence and wave spectrum on the thrust force is also investigated. The derived control structures are trained by system identification or artificial neural network techniques to achieve a simulation model and a prediction model separately.

The paper is structured as follows: In section 2, the classic model used to undertake the aero-hydro-servo-elastic coupled simulations are described. Section 3 lists the environmental conditions used to conduct the aero-hydro-servo-elastic coupled simulations. In Section 4, the methodology regarding the mathematical expression of the fully-coupled six motions of the platform, hydrodynamic calculation, aerodynamic calculation, mooring modelling, control and

111 electrical-drive are described in details. The analyses of the simulation result in various coupled
112 wave and wind conditions calculated by FAST, as well as the process of how to obtain the two
113 models are presented and discussed in Section 5. Section 6 summarises the conclusions from
114 the study.

115 2. Model description

116 The spar-buoy concept -"Hywind" floating wind turbine is initially developed by Statoil of
117 Norway. Then by NREL, aspects of the original data are adjusted slightly to make the platform
118 appropriate for supporting the NREL 5-MW baseline turbine. To differ from Statoil's original
119 Hywind concept, it is referred to as "OC3-Hywind". The OC3-Hywind floating wind turbine
120 concept is considered as the model in this study. We use the turbine specifications of the
121 National Renewable Energy Laboratory (NREL) offshore 5-MW baseline wind turbine, as
122 given in reference [7, 24]. Moreover, Fig.1 presents a model built from the data reflecting the
123 floating system properties documented in[7]. Seen in Fig. 3, a spar type platform is used to
124 carry the wind. Table 1 lists the specification details of the model

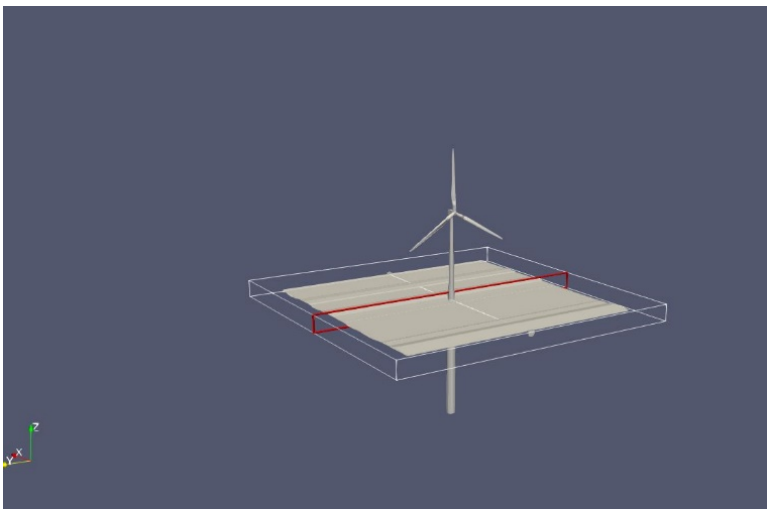

125
126 **Fig. 3 Building up the model for simulation**

127 **Table 1 General properties of the model**

Item	Value
Rating	5 MW

Rotor configuration	Upwind, three blades
Cut-in, rated,cut-out wind speed	3m/s,11.4m/s, 25m/s
Total draft below sea water level(SWL)	120m
Height to the base above SWL (top of platform)	10m
Height to Tower Top (Yaw Bearing) Above SWL	87.6m
The position of tower CM above SWL Along Tower centerline	43.4m
Tower Structural-Damping Ratio (All Modes)	1%
Nacelle dimension(length,width, height)	14.2m, 2.3m, 3.5m
Platform diameter above the taper	6.5m
Platform diameter below the taper	9.4m
Rotor nacelle assembly(RNA)mass	350000kg
Tower mass	249718kg
Platform mass, Including ballast	7466000kg
CM Location Below SWL Along Platform Centerline	89.9155 m
Platform Roll Inertia about CM	4,229,230,000 kg•m^2
Platform Pitch Inertia about CM	4,229,230,000 kg•m^2
Platform Yaw Inertia about Platform Centerline	164,230,000 kg•m^2
Number of mooring lines	3
Angle Between Adjacent Lines	120º
Depth to fairleads below SWL	70m
Depth to Anchors Below SWL	320m
Radius to Anchors from Platform Centerline	853.87m
Radius to Fairleads from Platform Centerline	5.2m
Unstretched Mooring Line Length	902.2m
Mooring Line Diameter	0.09 m
Equivalent Mooring Line Mass Density	77.7066 kg/m
Equivalent Mooring Line Weight in Water	698.094 N/m
Equivalent Mooring Line Extensional Stiffness	384,243,000 N
Additional Yaw Spring Stiffness	98,340,000 Nm/rad
Baseline control in Region 3	GSPI and constant torque

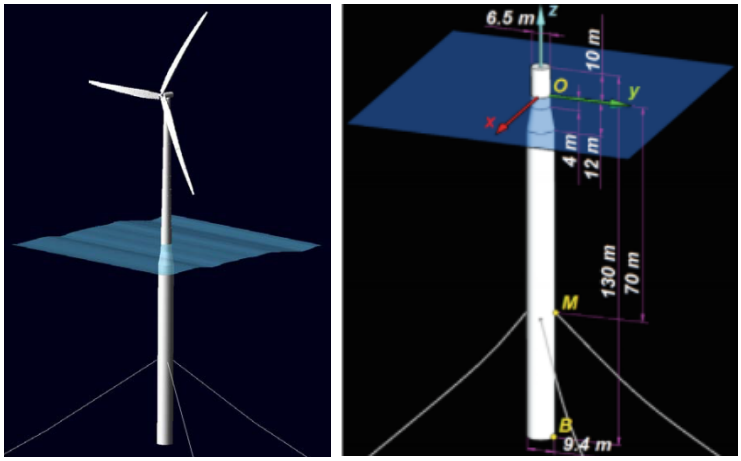

Fig. 4 Dimensions of the floating system

As shown in Fig. 4, the tower base overlaps with the top of the platform and is located 10 m above the static water level (SWL). Although the top of the tower protrudes with the yaw bearing, it is situated at 87.6m above SWL. The distribution characteristics of the tower are based on the base diameter of 6.5m, which is matched with the top width of the platform. Moreover, the base thickness of the tower is 0.027m, top diameter 3.87m, thickness 0.019m.

The tower is 10 meters above the SWL and cantilever to the top of the floating platform, which is considered rigid. A 3-leg catenary moors the model and the mooring system is spread with a delta connection. However, in the calculation, the delta connection is eliminated, and the mooring system is modified with a yaw spring to meet the proper general yaw stiffness.

3. Load cases

Table 2 lists all the load cases used in the simulation. In order to observe the effect of the waves on thrust, LC 1 consists of 35 separate simulations in regular wave conditions of different wave frequency. Likewise, to investigate the effect of wind speed on thrust, LC 2 is selected. To further observe the performance of thrust in the sophisticated natural environment, LC 3 is considered. To investigated the influence the turbulence and wave spectrum has on real-time

148 thrust, LC4-LC are included as comparative load cases. For each simulation, it runs 600s to get
149 an observation of the steady effect. However, only the data of 300s-500 s is selected for statistic
150 calculation and analyses in section 5.1 and 5.2, to get rid of the transient effect arising in the
151 initial simulation stage.

152 **Table 2 List of all the load cases used in the simulation**

Load Case	Enabled DOFs	Wave Conditions	Wind Conditions
LC1	Platform(floater), tower, drivetrain, blades	Regular airy: H=2m, ω=0.1, 0.2, …, 3.5 rad/s	Steady, no shear u=8 m/s
LC2	Platform, tower, drivetrain, blades	Regular airy: H=2m ω=0.5 rad/s	Steady, no shear u=2, 4, …,18 m/s
LC3	Platform, tower, drivetrain, blades	JONSWAP spectrum H_s=4.55 m, T_p =9.00s, γ=2.45	IECKAI model $\bar{u}$ =11.40 , TI=20.45
LC4	Platform, tower, drivetrain, blades	JONSWAP spectrum H_s=1.5 m, T_p =6.61s, γ=1.00	IECKAI model $\bar{u}$ =11.40 , TI=20.45
LC5	Platform, tower, drivetrain, blades	JONSWAP spectrum H_s=4.55 m, T_p =9.00s, γ=2.45	Steady, no shear u=11.40 m/s
LC6	Platform, tower, drivetrain, blades	JONSWAP spectrum H_s=1.5 m, T_p =6.61s, γ=1.00	Steady, no shear u=11.40 m/s

153

154 To simulate the natural environment, the sea states at the proposed site is characterised by the
155 JONSWAP spectrum, which is described as follow in a lecture of MIT
156 OpenCoursWare[25]:

157 $$S(\omega)=\frac{\alpha g^2}{\omega^5}\exp\{-1.25\left(\frac{\omega_p}{\omega}\right)^4\}\gamma^{\exp(-0.5(\frac{\omega-\omega_p}{\sigma\omega_p})^2)}$$ **Equation 1**

158 where, $\alpha=5.061\left(\frac{\omega_p}{2\pi}\right)^4 H_s^2[1-0.287\log\gamma]$; $\sigma=0.07$ for $\omega<\omega_p$, and $\sigma=0.09$ for $\omega\geq\omega_p$;

159 $\omega_p=2\pi/T_p$. H_s is the significant wave frequency, ω_p is the peak frequency, γ is the peak

160 enhance coefficient.

161 Moreover, for the wind field with a turbulent inflow, the IEC Kaimal spectral turbulent model

162 is used to characterise the wind conditions. When the atmospheric stability is aero, the spectra

163 for the three wind components, $K=u,v,w$ (u is horizontal wind speed) are as follow[26]:

164 $$S(f)=\frac{4\sigma_K^2 L_K/\bar{u}_{hub}}{\left(1+6fL_K/\bar{u}_{hub}\right)^{5/3}}$$ **Equation 2**

165 where f is the cyclic frequency and L_K is an integral scale parameter, which is defined as:

166 $$L_K=\begin{cases}8.10\Lambda_U, K=u\\ 2.70\Lambda_U, K=v\\ 0.66\Lambda_U, K=w\end{cases}$$

167

168 According to IEC 61400-3 code, the turbulence scale parameter $\Lambda_U=0.7\cdot\min(60m,H_{hub})$.

169 However, because $H_{hub}=90m$, then $\Lambda_U=42$. The relationships between the standard deviations

170 are established to be: $\sigma_v=0.8\sigma_u$, $\sigma_w=0.5\sigma_u$, $\sigma_u=\frac{TI}{100}\bar{u}_{hub}$, TI is the turbulence intensity, $\bar{u}_{hub}$

171 is the mean (total) wind speed at the reference height. Then the wind spectrum of LC 3 and LC

172 4 is as shown in Fig. 5.

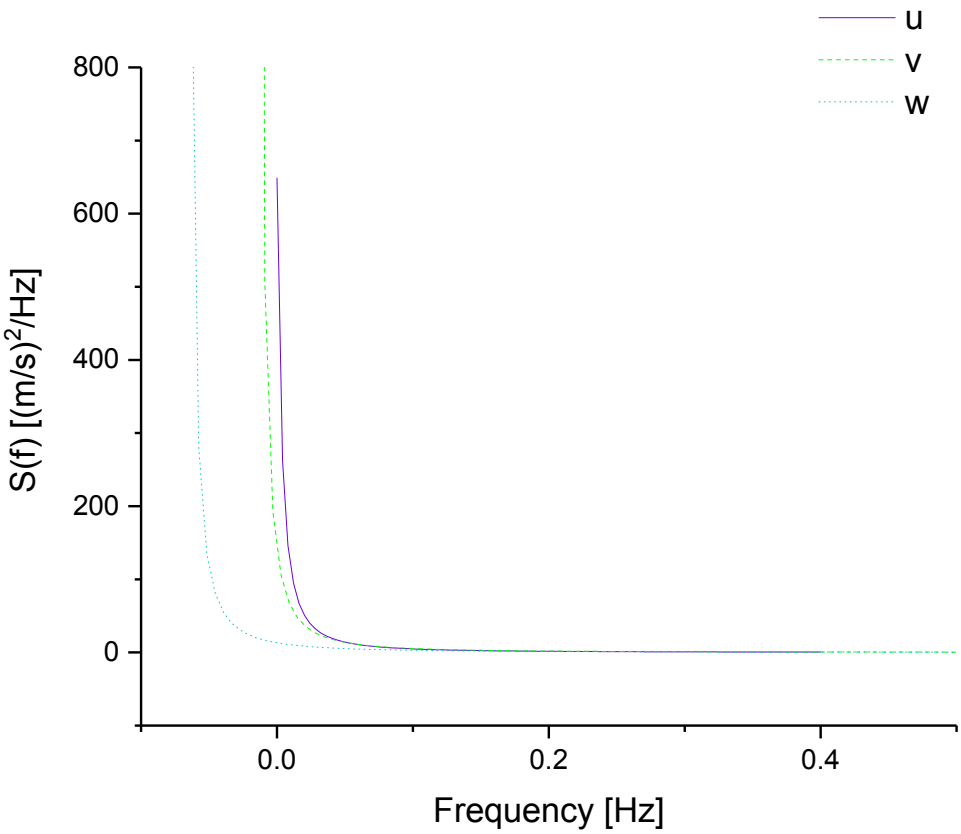

173

174 **Fig. 5 Spectrum of the wind adapted in LC 3&4**

175 ## 4. The methodology of the simulations

176 To predict the sophisticated dynamics of the spar-type floating wind turbine, a coupled aero-
177 servo-hydro-elastic model which integrates wind-inflow, the turbine control system (servo),
178 hydrodynamic and structural-dynamic (elastic) models is adapted to run the simulations.

179 ### 4.1 Fully coupled six motions

180 When the fully dynamic coupling between the floating foundation and the wind turbine is taken
181 into consideration, the coupled motions of the floating foundation in the time domain is
182 expressed as follow[27]:

183 $$M_{ij}(q,u,t)\ddot{q}_j = F_i(q,\dot{q},u,t) \qquad \textbf{Equation 3}$$

where q is the input of the six DOFs (heave, sway, surge, roll, pitch and yaw); u is the control inputs; M_{ij} is the (??, ??) component of the inertia mass matrix; $\ddot{q}_j$ is the acceleration of DOF ??; $\dot{q}$ is the velocity input of the DOFs; F_i is the force applied on DOF i.

Because of the balance of forces for the system, the total force applied to the system should be as follow:

$$*F_i + F_i = 0 \qquad \textbf{Equation 4}$$

where $*F_i = *F_i^{Hub} + *F_i^{Nacelle} + *F_i^{Tower} + *F_i^{Floater} + *F_i^{Blades}$;

$$F_i = F_i^{Aero} + F_i^{Hydro} + F_i^{Gravity} + F_i^{Elastic} + F_i^{Drivet} + F_i^{Mooring}.$$

4.2 Hydrodynamic methodology

In this study, both regular waves, and irregular (JONSWAP spectrum) waves are generated to form the coupled load conditions. Airy wave theory is adopted to model the wave kinematics, including both regular and irregular waves. For regular waves, the wave elevation (ζ) is represented as a sinusoid with a single amplitude (wave height) and frequency. Irregular is expressed as a summation or superposition of multiple wave components, as described by an appropriate wave spectrum[26]:

$$\zeta(t) = \frac{1}{2\pi}\int_{-\infty}^{\infty} W(\omega)\sqrt{2\pi S_{\zeta}^{2-sided}(\omega)}e^{j\omega t}d_{\omega} \qquad \textbf{Equation 5}$$

where, $W(\omega)$ is the Fourier transform of a realisation of a white Gaussian noise time-series process with zero mean and unit variance. This equation represents the wave elevation as an inverse Fourier transform of the desired two-sided power spectral density, $S_{\zeta}^{2-sided}$ where j is an imaginary number, and ω is an individual wave frequency.

Potential-flow theory and strip theory (via Morison's equation) are used to model the hydrodynamic loads. The forces acting on the floater (floating foundation) consist of diffraction,

radiation and hydrostatic forces as well as the restoring forces from the mooring lines and the added inertia of the fully coupled turbine. Therefore, the total external load acting on the floating foundation $F_i^{Floator}$ is described as follow:

$$F_i^{Floator} = -A_{ij}\ddot{q}_j + F_i^{Hydro} + F_i^{Mooring} \quad \textbf{Equation 6}$$

where, A_{ij} is the (??, ??) component of the added mass matrix, F_i^{Hydro} is the ith component of the applied hydrodynamic load on the floating foundation, $F_i^{Mooring}$ is the ith component of the load on the floating foundation from the mooring lines.

However, F_i^{Hydro} consists of three parts: radiation, diffraction and hydrostatic, hence:

$$F_i^{Hydro} = F_i^{Excitation} + F_i^{Hydrostatic} - F_i^{Radiation}$$

where, $F_i^{Excitation}$ is the total excitation load from incident waves, which is the result of the undisturbed pressure field (Froude-Krylov) and wave scattering (diffraction loads), $F_i^{Hydrostatic}$ is the restoring forces of a freely moving body. $F_i^{Radiation}$ is steady-state hydrodynamic forces and moments. Thus we get

$$F_i^{Hydrostatic} = \rho g V \delta_{i3} - C_{ij}^{Hydrostatic} q \quad \textbf{Equation 7}$$

$$F_i^{Radiation} = \int_0^t K_{ij}(t-\tau)\dot{q}_j(\tau)d_\tau \quad \textbf{Equation 8}$$

$$F_i^{Hydro} = F_i^{Excitation} + \rho g V \delta_{i3} - C_{ij}^{Hydrostatic} q_j - \int_0^t K_{ij}(t-\tau)\dot{q}_j(\tau)d_\tau \quad \textbf{Equation 9}$$

where $\rho g V \delta_{i3}$ is the buoyancy force from Archimedes' principle; thereof, δ_{i3} is the (i,3) component of the Kronecker-Delta function; $-C_{ij}^{Hydrostatic} q_j$ is the hydrostatic and torque variations resulting from the effects of the water-plane area and the COB; thereof, $C_{ij}^{Hydrostatic}$ is the (??,??) component of the linear hydrostatic restoring matrix; K_{ij} is the wave radiation retardation kernel - the impulse-response function of the radiation problem; t is the Simulation time; τ is the user variable time.

4.3 Aerodynamic methodology

In this study, both steady wind fields and turbulent wind fields are generated to couple with different wave conditions. For the convenience of describing the wind field, it is assumed that the inflow wind direction is horizontal as shown in Fig. 6. Power-Law wind profile is used to determine the mean *u*-component velocity at each height in the wind filed.

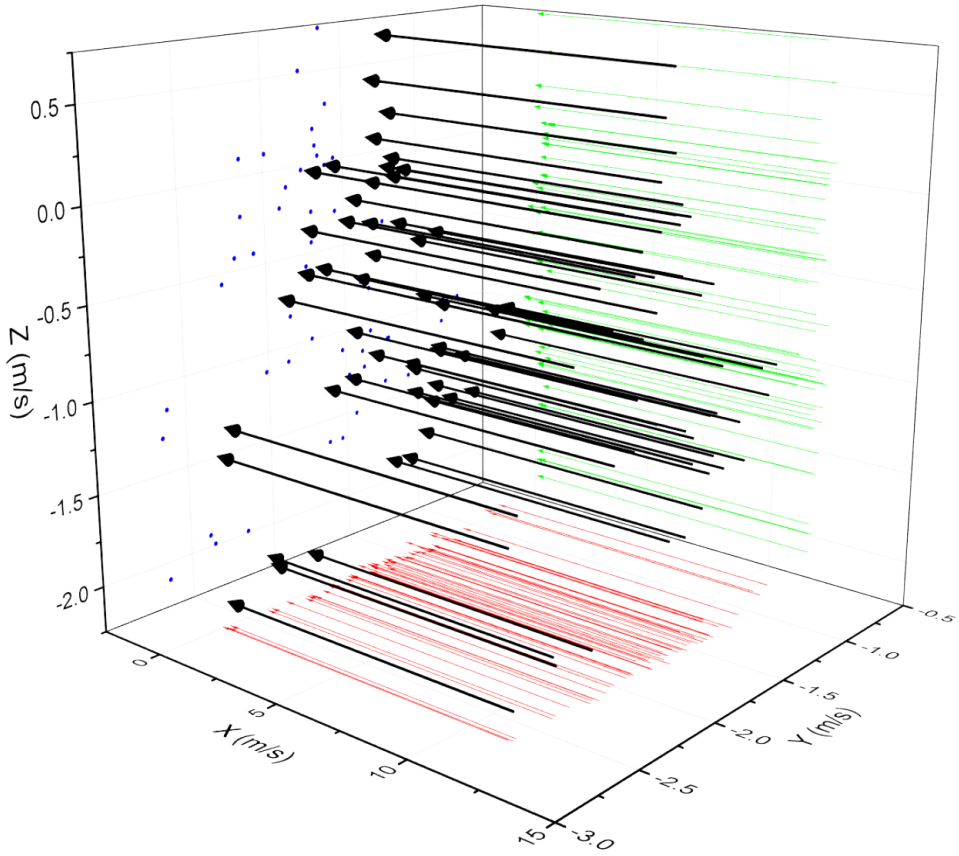

Fig. 6 The global coordinate system concerning the turbulent wind

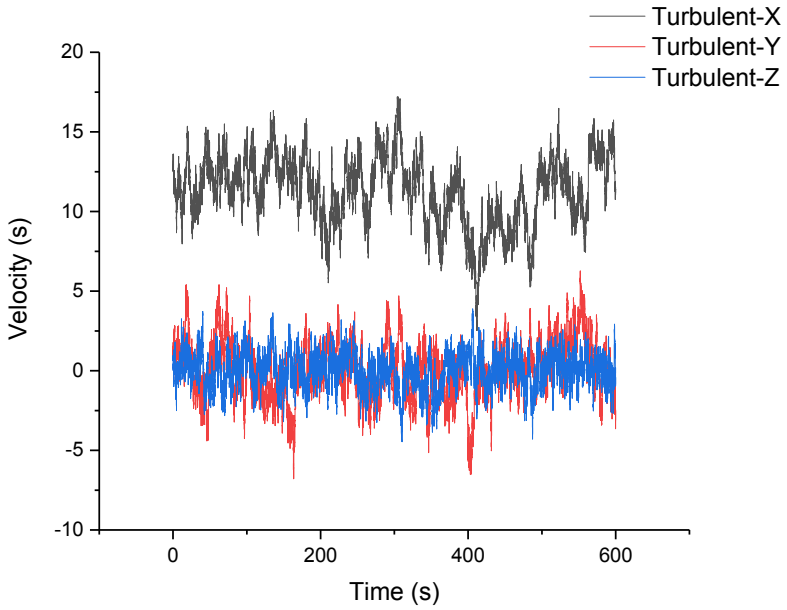

235

236 **Fig. 7 History of wind speed in the turbulent wind field**

237 As discussed in section 3, Fig. 5 displays the spectrum of turbulent wind. Moreover, Fig. 7
238 plots the history of wind speed. As shown in Fig. 7, the slow slow-varying component forms
239 the turbulence. However, in the natural world, not only the amplitude of the wind speed varies,
240 but also the speed direction is time-dependent. For analysis purposes, coherent structures have
241 been defined regarding coherent turbulent kinetic energy (CTKE), and the turbulent kinetic
242 energy (TKE) is used to model the power spectrum as shown in Fig. 8.

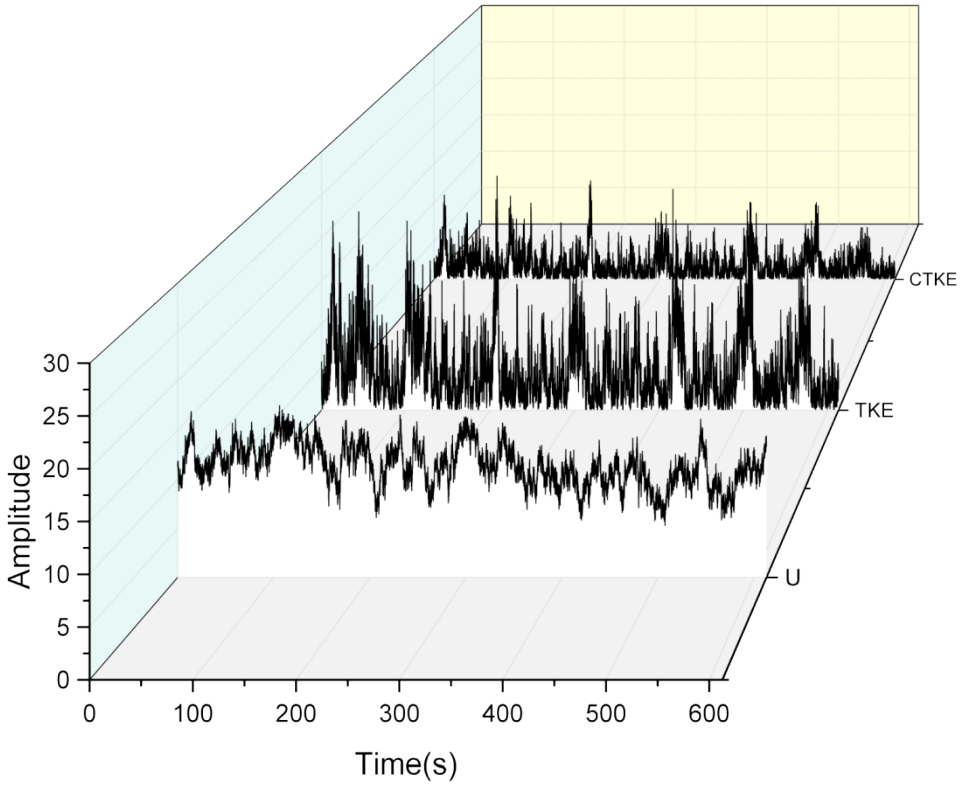

243

244 **Fig. 8 Energy distribution along the turbulent velocity**

245 ## 4.4 Mooring modelling

246 For mooring modelling, the closed–form solution[28] of the classic single line is reformulated
247 into a piecewise, multi-segmented system as shown in Fig. 9 (where r_i is the node position
248 vector, $x_i z_i$ is a local frame, XYZ is the global coordinate system). This piecewise system is
249 composed of a collection of nodes and elements. The mean forces in the mooring system,
250 including elasticity, weight (in fluid), and geometric nonlinearities, are accounted.

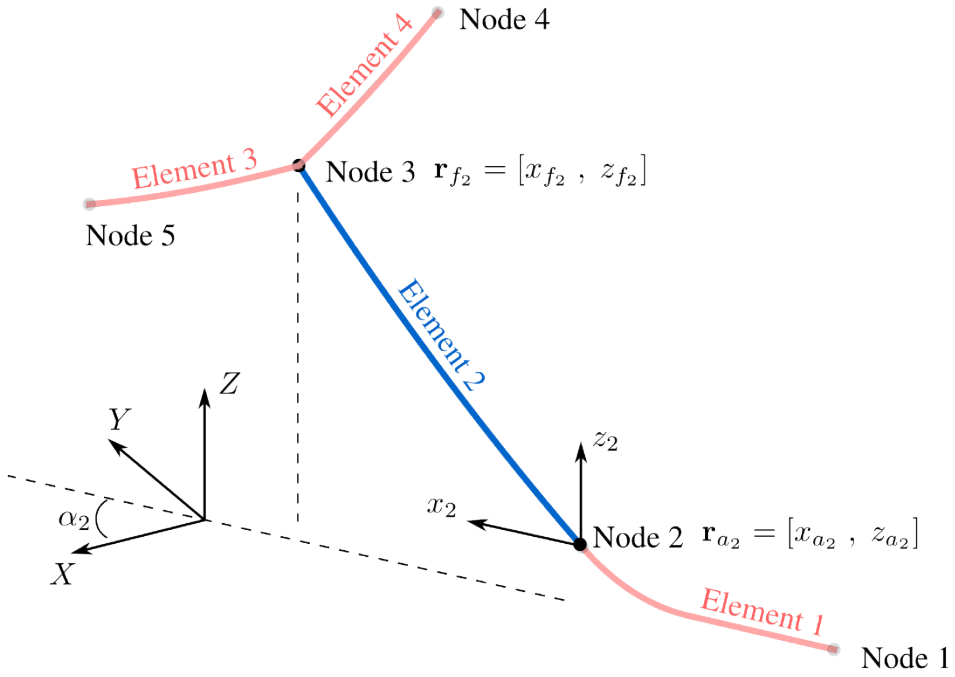

Fig. 9 the piece-wise, the multi-segmented system of a classic mooring line[29]

The solution process begins with the evaluation of the two continuous analysis catenary equations of each element based on the horizontal and vertical orifice offsets obtained through the nodal displacement relationship. The element is defined as a component that connects two adjacent nodes. Evaluating the force balance equation for each node as follow:

$$\{F\}_X^j = \sum_{i=1}^{n}[H_i\cos(\alpha_i) - F_{X_j}^{ext}] = 0$$

$$\{F\}_Y^j = \sum_{i=1}^{n}[H_i\sin(\alpha_i) - F_{Y_j}^{ext}] = 0 \qquad \textbf{Equation 10}$$

$$\{F\}_Z^j = \sum_{i=1}^{n}[V_i] - F_{Z_j}^{ext} + M_j g - \rho g B_j = 0$$

where, H is the horizontal fairlead force, V is the vertical fairlead force, $n = 1,2,...$ is the elements at the node j, F^{ext} is the external force in the global coordinate system. Once the element fairlead (H,V) and anchor (H_a,V_a) values are known at the element level, their contribution at each element's anchor and fairlead are obtained by Equation 13.

4.5 Control and electrical-drive modelling

A conventional variable-speed, variable blade-pitch-to-feather control modelling strategy is usually used for onshore NREL 5-MW turbines, and an example of the steady-state behaviour of onshore NREL 5-MW turbine under operational control is given in Fig. 10 (where 'RotSpeed' is for rotor speed, 'BldPitch1' is for the pitch angle for blade 1, 'GenTq' is for generator torque, and 'TSR' is for tip-speed ratio). However, the conventional pitch-to-feather control usually results in a reduction of the steady-state rotor thrust when increase wind speed above rated, when applied on a floating wind turbine as discussed by Nielsen et al. in [30, 31].

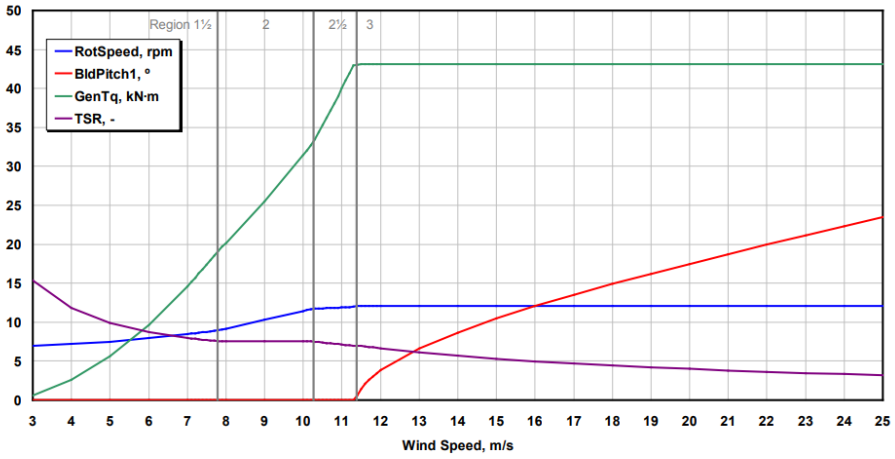

Fig. 10 Steady-State behaviour of onshore NREL 5-MW turbine under operational control[32]

Therefore, in this research, two modifications are adapted as listed in Table 3, and a time step is added for the Bladed-style DLL controllers, which is independent of the ServoDyn time step. Moreover, a linear ramp and first-order low-pass filter are applied to the blade-pitch command from the Bladed-style DLL.

Table 3 Control System Property Modifications[32]

Proportional Gain at Minimum Blade-Pitch Setting	0.006275604 s
Integral Gain at Minimum Blade-Pitch Setting	0.0008965149
Constant (Rated) Generator Torque in Region 3	43,093.55 $N \cdot m$

5. Results

This section provides the analyses of data from simulations and proposes two models. The simulation model of the thrust acting on the rotor is obtained by the data from LC1 and LC 2; the simulation model is estimated by system identification techniques regarding high frequency and low-frequency response separately to account the dominating influence. The prediction model is obtained by artificial neural network method to train a black box by the data from simulations of LC 3-LC 6.

5.1 Rotor thrust prediction under LC 1

In this section, the wind speed of uniform wind field is 8m/s, and 35 frequencies of 0.1 -3.5 rad/s of regular waves with a constant wave height of 2m, are used to run the simulations. The outputs of one standard simulation are shown in Fig. 11. As pointed out in [33, 34]], the same phenomenon is observed from the series simulation, that for numerous environmental condition, the significant response is the surge and pitch motions. Moreover, thrust is fundamentally due to the relative wind speed experienced by the turbine blades. For example, if the platform is fixed, then the relative wind speed experienced by the edges will be the same as the actual wind speed.

However, for a floating wind turbine, the platform is moving back and forward relative to the wind, and in this case, the turbine blades experience the relative wind speed. Since we are only looking at wind and wave direction in the x-axis, then the platform motions are predominately pitched and surge, i.e. roll, yaw, sway is practically zero as shown in Fig. 11. When the platform pitches or surges this adds a component to the relative wind speed. Hence when predicting the thrust for a floating wind turbine, the authors would like to use surge, pitch (which provide the corresponding component of wind) and the actual wind speed. Therefore, the surge and pitch

motions of the platform are extracted from the outputs to observe their correlation with the aerodynamic thrust in this section.

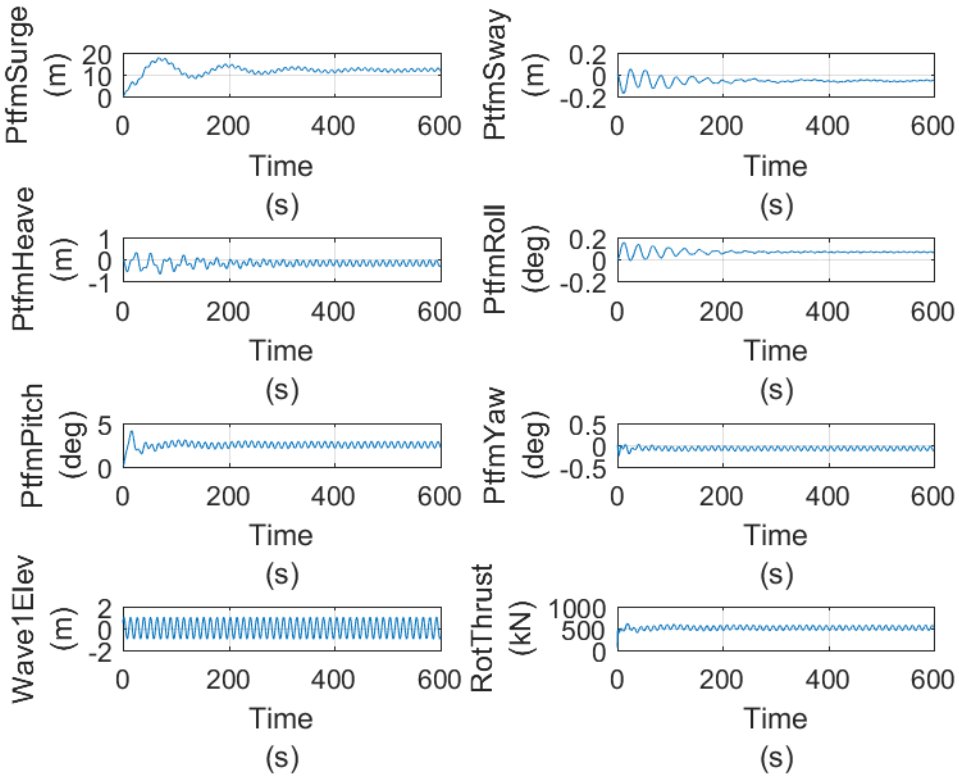

Fig. 11 Some outputs from one standard simulation under ω=0.5 rad/s, u=8 m/s

To observe the correlation between Surge, pitch, and thrust, two 4th order Buttherworth filters are designed to separate the thrust, surge, and pitch signals into two independent components (high-frequency component and low-frequency component), respectively. The cut-off frequency for both high pass filter and low pass filter is 0.01 Hz, to include all the data of the three signals (surge, pitch, and thrust). Also, the transfer function is expressed regarding b and a as:

$$H(z)=\frac{B(z)}{A(z)}=\frac{b(1)+b(2)z^{-1}+b(3)z^{-2}+b(4)z^{-3}+b(5)z^{-4}}{a(1)+a(2)z^{-1}+a(3)z^{-2}+a(4)z^{-3}+a(5)z^{-4}} \quad \textbf{Equation 11}$$

where, b and a are the transfer function coefficients of the 4th-order filters. And $b=[0.9990,-3.9959,5.9938,-3.9959,0.9990]$, $a=[1.0000,-3.9979,5.9938,-3.9938.0.9979]$

for the high pass filter; $b=[2.3759,9.5035,14.2550,9.5035,2.3759]\times10^{-14}$, $a=[1.0000,-3.9979,5.9938,-3.9938,0.9979]$ for the low pass filter. Once the filters designed, the three signals are separated. One example when ω=1.9 rad/s, u=8 m/s is given in Fig.9(see separation analyses for other cases in the supplementary dataset). Fig. 12 illustrates that the filters are effective to separate the properties of the original signal into two independent parts.

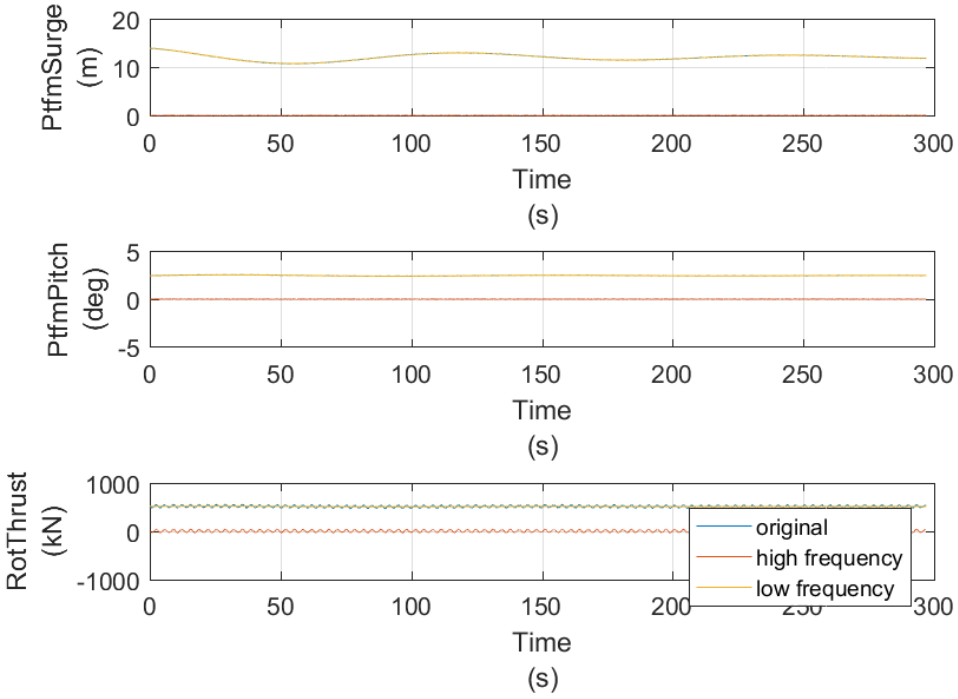

Fig. 12 Separation of the three signals at ω=1.9 rad/s, u=8 m/s

wind	wave			surge_high		pitch_high		thrust_high		surge_lo	pitch_low	thrust_low
wind(m/s)	w(rad/s)	f(Hz)	Hs(m)	H(m)	f(Hz)	A(deg)	f(hz)	T(KN)	f(hz)	H(m)	A(deg)	T(KN)
8	0.2	0.032	2	1.49	0.033	0.133	0.031	11.969	0.033	11.817	2.422	504.803
8	0.5	0.08	2	1.504	0.080	0.760	0.080	116.955	0.086	11.963	2.455	506.259
8	0.7	0.111	2	0.859	0.111	0.098	0.111	37.112	0.112	11.951	2.449	505.373
8	0.9	0.143	2	0.509	0.142	0.076	0.142	42.554	0.143	11.983	2.449	505.133
8	1.2	0.191	2	0.249	0.188	0.049	0.188	49.369	0.195	11.936	2.445	504.777
8	1.5	0.239	2	0.119	0.236	0.029	0.235	51.131	0.243	11.962	2.446	504.705
8	1.6	0.255	2	0.090	0.254	0.024	0.250	50.143	0.263	11.957	2.446	504.722
8	1.9	0.302	2	0.040	0.298	0.012	0.295	46.066	0.302	11.958	2.446	504.711
8	2.2	0.35	2	0.018	0.334	0.006	0.342	43.475	0.350	11.966	2.447	504.744
8	2.5	0.398	2	0.012	0.556	0.005	0.386	44.313	0.397	11.950	2.445	504.512
8	2.9	0.462	2	0.020	0.455	0.011	0.453	63.071	0.461	11.958	2.446	504.636
8	3.5	0.557	2	0.014	0.548	0.009	0.547	24.485	0.558	11.961	2.446	504.691

Fig. 13 the separated components of the surge, pitch, and thrust for a range of ω at the wind speed of 8m/s

The static calculation results of the separated components for all simulations included in load cases 1 are shown in Fig. 13. Looking at results, it is noticed that low-frequency components of the three signals (surge_low, pitch_low, thrust _low) tend to be independent on wave frequency. However, the high-frequency components (surge_high, pitch_high, thrust _high) tend to be dependent on the wave frequency. Therefore, if surge_RAO, pitch_RAO and thrust_RAO are defined as follow :

$$surge\_RAO = \frac{surge}{Hs} \quad \textbf{Equation 12}$$

$$pitch\_RAO = \frac{pitch}{Hs} \quad \textbf{Equation 13}$$

$$thrust\_RAO = \frac{thrust}{120} \quad \textbf{Equation 14}$$

where, Hs is the significant wave height, 120 is the introduce scaling coefficient. Thus, the RAOs are presented in Fig. 14.

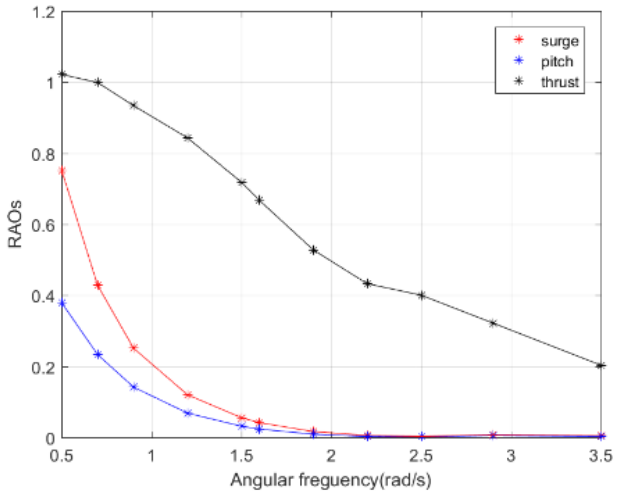

Fig. 14 the RAOs of the surge, pitch, and thrust at a range of ω at the wind speed of 8m/s

It is noticed in Fig. 14, there might be a linear correlation between thrust _high, surge_high and pitch_high when the wave frequency increase. Then the structure of the mathematical

model to predict the high-frequency component of the aerodynamic thrust is assumed to be as:

$$RAO\_thrust\_high = k_1 \times RAO\_pitch\_high + k_2 \times RAO\_surge\_high + c(\omega) \quad \textbf{Equation 15}$$

where k_1, k_2 are model parameters, and $c(\omega)$ is a constant modification relative to wind speed(see section 5.1.2), which could be identified by using the data of inputs(RAO_surge_high, RAO_thrust_high) and outputs($thrust\_RAO\_high$).

5.2 Rotor thrust under LC 2

As learned from above, the high-frequency component of the three observed signals are independent of wave frequencies, in this section, the frequency of regular waves (airy) is 0.5 rad/s, and velocities of u=2, 4, …,18 m/s of steady wind, are used to run the simulations, for observing the effect of wind speed on aerodynamic thrust. One example of the simulation at ω =0.5 rad/s, u=12m/s after applying the data through the high pass and low pass filters is shown in Fig. 15

wind	wave			surge_high		pitch_high		thrust_high		surge_low	pitch_low	thrust_low
wind(m/s)	w(rad/s)	f(Hz)	Hs(m)	H(m)	f(Hz)	A(deg)	f(hz)	T(KN)	f(hz)	H(m)	A(deg)	T(KN)
2	0.5	0.08	2	1.474	0.080	0.732	0.080	97.768	0.080	1.102	0.196	134.074
4	0.5	0.08	2	1.477	0.080	0.736	0.080	103.036	0.080	3.763	0.761	225.799
6	0.5	0.08	2	1.487	0.080	0.746	0.080	113.295	0.080	7.355	1.508	347.780
8	0.5	0.08	2	1.504	0.080	0.760	0.080	116.955	0.086	11.973	2.456	506.397
10	0.5	0.08	2	1.497	0.081	0.775	0.079	133.277	0.087	18.030	3.707	724.560
12	0.5	0.08	2	1.352	0.081	0.672	0.079	184.146	0.083	20.070	4.121	792.488
14	0.5	0.08	2	1.356	0.081	0.673	0.079	167.927	0.083	16.023	3.286	634.720
16	0.5	0.08	2	1.368	0.079	0.672	0.078	161.980	0.087	13.850	2.840	556.172
18	0.5	0.08	2	1.362	0.079	0.670	0.078	162.021	0.087	12.524	2.563	507.111

Fig. 15 the separated components of the surge, pitch, and thrust for a range of u at the ω=0.5 rad/s

Similarly, the static calculation of the separated components for all simulations included in load cases 2 is carried out, and the results are listed in Fig. 15. Different from being independent of wave frequencies, the low-frequency components of the three signals vary dramatically as the wind speed changes. As the RAOs of the three signals are defined above, the analyses carried out all based on RAOs in the section, as shown in Fig. 16. Learn from Fig. 16(a), the

high-frequency components of surge and pitch tend to be steady when the wind speed increase, while the high- requency thrust component increses slightly, which is primarily described by the $c(u)$ in the structure of the mathematical model. So when Equation17 modified with an offset the structure represented by equation 17 can predict the high-frequency component when wind speed changes. Therefore, the fabric used to predict the thrust-high is modified as:

$$RAO\_thrust\_high = k_1 \times RAO\_pitch\_high + k_2 \times RAO\_surge\_high + c(\omega) + c_1$$

Equation 16

where, c_1 is a constant offset related to wind speed.

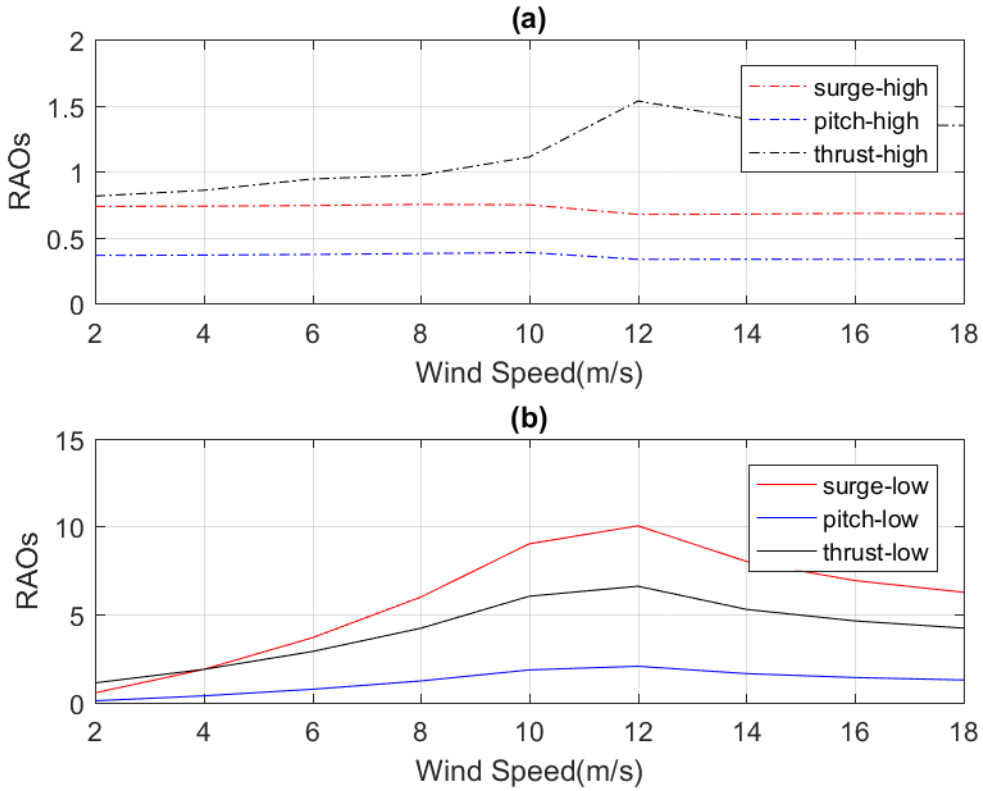

Fig. 16 Behaviours of the high or low components of the surge, pitch, and thrust at a range of wind speed at ω =0.5 rad/s

Additionally, it is observed in Fig. 16(b) that there is an apparent linear correlation among surge_low, pitch_low, thrust _low when the wind speed increase from 2m/s to 8m/s, and they all reach the maximum when the wind speed is 12m/s. Therefore the structure of the

mathematical model to predict the low-frequency component of aerodynamic thrust is assumed to be as:

$$RAO\_thrust\_low = k_3 \times RAO\_pitch\_low + k_4 \times RAO\_surge\_low + k_5 \times wind\_speed + c_2 \quad \text{Equation 17}$$

where k_3, k_4, k_5 are also model parameters, but different from k_1, k_2, and c_2 is an allowable constant offset to make up the uncertainty might result from the linear structure. And it will be identified by using the data of inputs(RAO_surge_high, RAO_thrust_high) and outputs($thrust\_RAO\_high$) as discussed below.

5.2 Training of the simulation model of rotor thrust

As discussed above, two structures (Equation 18&19) are obtained to predict the aerodynamic thrust:

$$RAO\_thrust\_high = k_1 \times RAO\_pitch\_high + k_2 \times RAO\_surge\_high + c(\omega) + c_1$$

$$RAO\_thrust\_low = k_3 \times RAO\_pitch\_low + k_4 \times RAO\_surge\_low + k_5 \times wind\_speed + c_2$$

For the simplicity of scientific discussion, RAO_pitch_high, RAO_surge_high are represented as inputs u_1, u_2, and RAO_pitch_low, RAO_surge_low as inputs $*u_1, *u_2$ to differ from, RAO_pitch_high RAO_surge_high. Similarly, the output $thrust\_RAO\_high$ will be discussed as Y_{low}, and Y_{high}. As the model structures and some input and output signals are obtained, the values of adjustable parameters in the given model structure could be estimated by minimising the error between the model output and the measured response. The output y_{model} of the linear model is provided by:

$$y_{model}(t) = Gu(t)$$

where G is the transfer function, $y_{model}(t)$ is the simulated response of the model for a given input u(t) (such as $u_1, u_2, *u_1, *u_2$). The principal of determining G is minimising the difference between the model output $y_{model}(t)$ and the measured output $y_{meas}(t)$ (such as Y_{low}, Y_{high}). The minimisation criterion is a weighted norm of the error, $v(t)$, where: $v(t) = y_{meas}(t) - y_{model}(t)$.

Therefore for Equation 18, the output $y_{model}(t)$ is related to four inputs in total, which are $RAO\_pitch\_high, RAO\_surge\_high, \omega, Y_{high}$ (discussed as $u_1, u_2\ u_3, u_4$). Then the transfer functions are obtained as follow:

From u_1 to y_{model}: $G_1(s) = \dfrac{864.9s - 107.4}{s^2 + 1.853s + 2.271}$

From u_2 to y_{model}: $G_2(s) = \dfrac{-266.6s + 90.01}{s^2 + 2.105s + 1.861}$

From u_3 to y_{model}: $G_3(s) = \dfrac{52.48s - 9.524}{s^2 + 5.725e^{-10}s + 1.374}$

From u_4 to y_{model}: $G_4(s) = \dfrac{-0.2402s + 1.105}{s^2 + 1.379s + 1.317}$

Fit to estimation data reaches 99.12%, the mean square error is 0.0206 when compared to the original signal.

For Equation 19, the output $y_{model}(t)$ is related to four inputs in total, which are $RAO\_pitch\_low, RAO\_surge\_low, wind\_speed, Y_{low}$ (discussed as $*u_1, *u_2\ *u_3, *u_4$). Then the transfer functions are obtained as follow:

From $*u_1$ to y_{model}: $G_1(s) = \dfrac{-19.72s + 2.124}{s^2 + 3.86s + 0.1255}$

From $*u_2$ to y_{model}: $G_2(s) = \dfrac{-4.211s + 2.433}{s^2 + 4.208s + 1.718}$

From $*u_3$ to y_{model}: $G_3(s) = \dfrac{3.712s - 0.2842}{s^2 + 1.407s + 1.009}$

From $*u_4$ to y_{model}: $G_4(s) = \dfrac{0.1383s - 0.1432}{s^2 + 0.04644s + 0.6857}$

5.3 Rotor thrust under LC 3-6 and the prediction model of rotor thrust

Real sea states are more sophisticated than regular-wave and steady-wind conditions. For LC3-LC4, JONSWAP spectrum and IECKAI turbulent model are adapted to characterise the environmental conditions, and corresponding simulations are undertaken. To observe the effect of turbulence inflow on the aerodynamic thrust, the identical steady wind cases (load cases 4.X) are simulated as well. The output of some significant response of LC3 is shown in Fig. 17

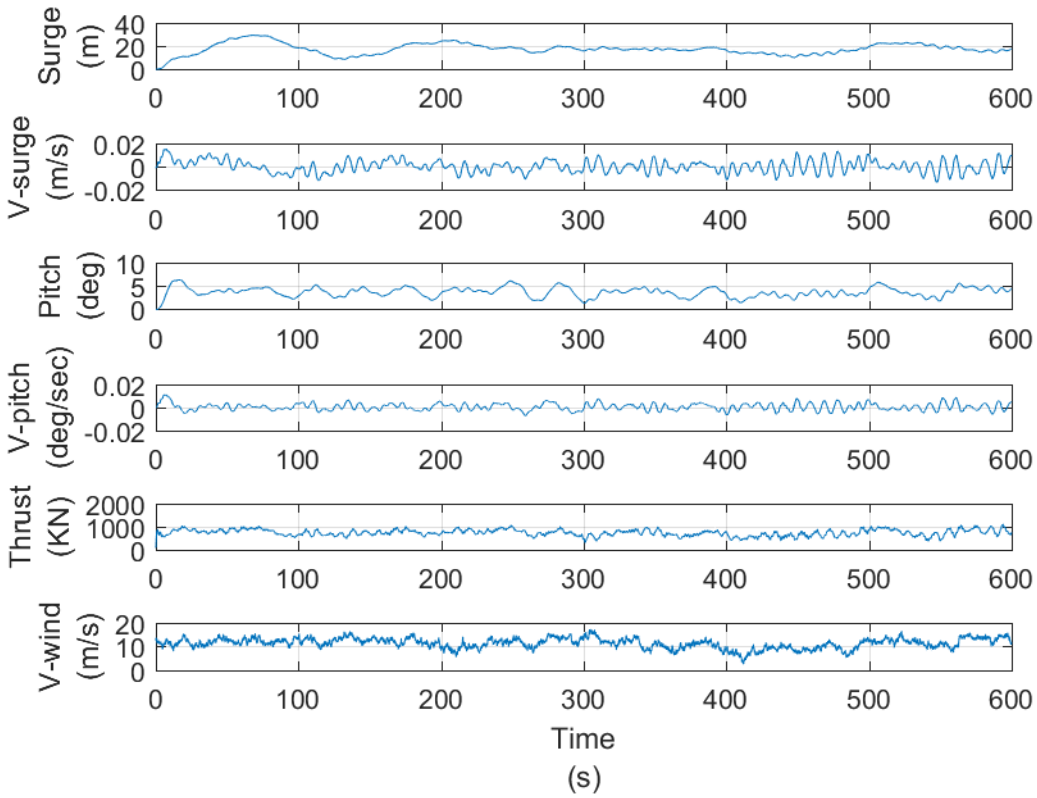

Fig. 17 Significant outputs from a simulation of LC 3

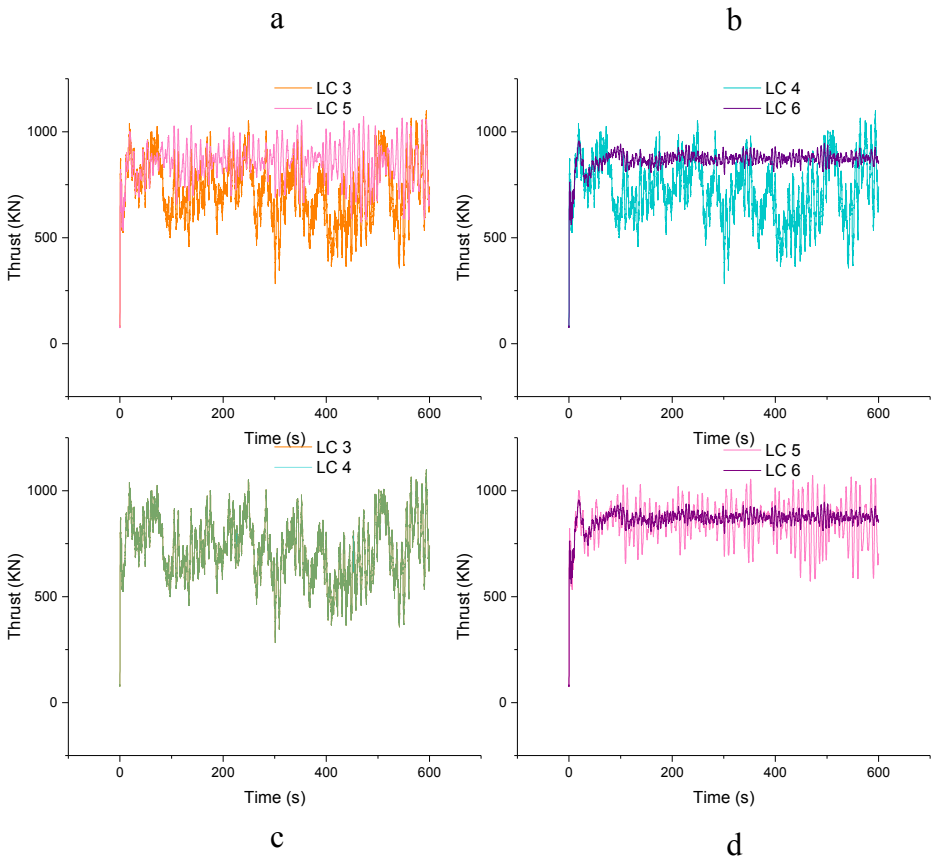

425

426 **Fig. 18 Thrust comparison of LC 3 -LC 6**

427 It is learned from Fig. 18(a & b) that the average thrust force is just slightly varied by the
428 turbulence. Although the inflow is turbulent, the mean wind speed of LC 3, LC 4 is identical
429 to that of the uniform wind field LC 5, LC 6. Therefore, the mean thrust force acting on the
430 rotor is nearly the same. Nevertheless, the thrust force becomes very unstable in the presence
431 of turbulence. Fig. 18(c) compares the thrust forces of identical turbulent inflows but different
432 wave spectrum parameters, and it is learned that in the presence of turbulence the influence of
433 wave changes on aerodynamic thrust are ignorable. However, as shown in Fig. 18(d), which
434 compares the thrust forces of identical steady wind inflow but different wave conditions, the
435 changes in parameters of wave spectrum have impacts on the behaviour of the thrust, though
436 the mean thrust force is almost the same. Therefore, data of five inputs are included in training
437 a model to predict the thrust force acting on the rotor for sophisticated environmental

conditions like LC 3-LC 6. If the model is written in the term of $A(z)y_{model}(t) = B(z)u(t) + e(t)$, the inputs

$u(t)$ includes the pitch($u_1(t)$), the velocity of pitch ($u_2(t)$), the surge($u_3(t)$), the velocity of surge, and the velocity of wind($u_5(t)$). Of course, $y_{model}(t)$ is the real-time thrust, $A(z)$ and $B(z)$ are the estimable parameters of the model. Thus one thrust force prediction model is obtained, e(t)is the noise source. The estimable parameters are as follow:

$$A(z) = 1 - 2.191z^{-1} + 1.884z^{-2} - 1.069z^{-3} + 0.5424z^{-4} - 0.3577z^{-5} + 0.2575z^{-6} - 0.08479z^{-7} - 0.001325z^{-8} + 0.04657z^{-9} - 0.02854z^{-10}$$

$$B_1(z) = 59.61z^{-1} - 330.3z^{-5} + 634.7z^{-6} - 364z^{-10}$$

$$B_2(z) = 99.66z^{-1} - 158.8z^{-3} - 119.6z^{-4} - 275.7z^{-5} - 584.1z^{-7} - 351.5z^{-8} - 29.44z^{-9}$$

$$B_3(z) = -51.46z^{-1} + 31.95z^{-4} + 30.17z^{-5} - 10.65z^{-10}$$

$$B_4(z) = -43.35z^{-1} + 24.39z^{-2} + 27.39z^{-3} - 4.442z^{-7} + 19.42z^{-8} + 50.99z^{-9} + 51.06z^{-10}$$

$$B_5(z) = -0.1884z^{-1} + 0.3314z^{-2} - 0.214z^{-3} + 0.3012z^{-4} - 0.4324z^{-5} + 0.4156z^{-6} - 0.2558z^{-7} + 0.115z^{-8} - 0.2601z^{-9} + 0.2063z^{-10}$$

Generally, the bigger the dataset is, the more accurate model will be obtained, and the model will slightly increase when the database reaches a certain level. For the model proposed in this paper, the size of the dataset is 192000. And the accuracy of fitting to estimate data is [98.88 98.73 99.84 99.69] %, and the mean square error is [2.396 2.336 0.02436 0.01664] respectively for LC3-LC6. The final prediction error for the above model is 1.194.

5 Conclusions

In this paper, numerous simulations based on the classic model of 'OC3-hywind' floating wind turbine have been carried out, and the data from simulations has been analysed in great details, Moreover, artificial neural network techniques are used to obtain the structure of the thrust force simulation and prediction models of the real-time thrust acting on the rotor of FOWTs. . It could be used as a software-in-the-loop application in the experiments to provide real-time thrust varying with the input signals(like surge, surge velocity, pitch, pitch_velocity, wind speed, wave condition ed.).

Reference

[1] J. Kaldellis and M. Kapsali, "Shifting towards offshore wind energy—Recent activity and future development," *Energy Policy,* vol. 53, pp. 136-148, 2013.

[2] P. power. (2017). *World's first floating wind farm has started production*.

[3] Y. Si, H. R. Karimi, and H. Gao, "Modeling and Parameter Analysis of the OC3-Hywind Floating Wind Turbine with a Tuned Mass Damper in Nacelle," *Journal of Applied Mathematics,* vol. 2013, p. 10, 2013.

[4] H.-J. Ahn and H. Shin, "Model test & numerical simulation of OC3 spar type floating offshore wind turbine," *International Journal of Naval Architecture and Ocean Engineering,* 2017/11/11/ 2017.

[5] H. Shin, "Model Test of the OC3-Hywind Floating Offshore Wind Turbine," presented at the The Twenty-first International Offshore and Polar Engineering Conference, Maui, Hawaii, USA, 2011.

[6] H. Shin, P. T. Dam, K. J. Jung, J. Song, C. Rim, and T. Chung, "Model test of new floating offshore wind turbine platforms," *International Journal of Naval Architecture and Ocean Engineering,* vol. 5, pp. 199-209, 2013/06/01/ 2013.

[7] J. Jonkman, *Definition of the Floating System for Phase IV of OC3*, 2010.

[8] H. R. Martin, R. W. Kimball, A. M. Viselli, and A. J. Goupee, "Methodology for wind/wave basin testing of floating offshore wind turbines," *Journal of Offshore Mechanics and Arctic Engineering,* vol. 136, p. 020905, 2014.

[9] A. J. Goupee, B. J. Koo, R. W. Kimball, K. F. Lambrakos, and H. J. Dagher, "Experimental comparison of three floating wind turbine concepts," *Journal of Offshore Mechanics and Arctic Engineering,* vol. 136, p. 020906, 2014.

[10] M. Jeon, S. Lee, and S. Lee, "Unsteady aerodynamics of offshore floating wind turbines in platform pitching motion using vortex lattice method," *Renewable Energy,* vol. 65, pp. 207-212, 2014.

[11] S. Quallen, T. Xing, P. Carrica, Y. Li, and J. Xu, "CFD simulation of a floating offshore wind turbine system using a quasi-static crowfoot mooring-line model," in *The Twenty-third International Offshore and Polar Engineering Conference*, 2013.

[12] A. J. Coulling, A. J. Goupee, A. N. Robertson, J. M. Jonkman, and H. J. Dagher, "Validation of a FAST semi-submersible floating wind turbine numerical model with

DeepCwind test data," *Journal of Renewable and Sustainable Energy,* vol. 5, p. 023116, 2013.

[13] T. Chujo, S. Ishida, Y. Minami, T. Nimura, and S. Inoue, "Model experiments on the motion of a spar type floating wind turbine in wind and waves," in *ASME 2011 30th International Conference on Ocean, Offshore and Arctic Engineering*, 2011, pp. 655-662.

[14] K. Müller, F. Sandner, H. Bredmose, J. Azcona, A. Manjock, and R. Pereira, "Improved tank test procedures for scaled floating offshore wind turbines," 2014.

[15] B. J. Koo, A. J. Goupee, R. W. Kimball, and K. F. Lambrakos, "Model tests for a floating wind turbine on three different floaters," *Journal of Offshore Mechanics and Arctic Engineering,* vol. 136, p. 020907, 2014.

[16] E. Oguz, O. University of Strathclyde. Department of Naval Architecture, and M. Engineering, *Hydrodynamic Design Aspects of Tension Leg Platforms for Wind Turbines*, 2016.

[17] Y. Liu, Q. Xiao, A. Incecik, C. Peyrard, and D. Wan, "Establishing a fully coupled CFD analysis tool for floating offshore wind turbines," *Renewable Energy,* vol. 112, pp. 280-301, 2017/11/01/ 2017.

[18] G. K. Y. Chan, P. D. Sclavounos, J. Jonkman, and G. Hayman, "Computation of nonlinear hydrodynamic loads on floating wind turbines using fluid-impulse theory," in *ASME 2015 34th International Conference on Ocean, Offshore and Arctic Engineering*, 2015, pp. V009T09A038-V009T09A038.

[19] Y. Bazilevs, M. C. Hsu, I. Akkerman, S. Wright, K. Takizawa, B. Henicke*, et al.*, "3D simulation of wind turbine rotors at full scale. Part I: Geometry modeling and aerodynamics," *International Journal for Numerical Methods in Fluids,* vol. 65, pp. 207-235, 2011.

[20] M. J. Fowler, R. W. Kimball, D. A. Thomas, and A. J. Goupee, "Design and testing of scale model wind turbines for use in wind/wave basin model tests of floating offshore wind turbines," in *ASME 2013 32nd International Conference on Ocean, Offshore and Arctic Engineering*, 2013, pp. V008T09A004-V008T09A004.

[21] I. Bayati, M. Belloli, D. Ferrari, F. Fossati, and H. Giberti, "Design of a 6-DoF robotic platform for wind tunnel tests of floating wind turbines," *Energy Procedia,* vol. 53, pp. 313-323, 2014.

[22] A. H. Day, D. Clelland, E. Oguz, S. Dai, J. Azcona Armendáriz, F. Bouchotrouch*, et al.*, "Realistic simulation of aerodynamic loading for model testing of floating wind turbines," 2017.

[23] M. Kraskowski, K. Zawadzki, and A. Rylke, "A Method for Computational and Experimental Analysis of the Moored Wind Turbine Seakeeping," in *Proceedings, 18th Australasian Fluid Mechanics Conference, Launceston, Australia*, 2012.

[24] J. Jonkman, S. Butterfield, W. Musial, and G. Scott, "Definition of a 5-MW reference wind turbine for offshore system development," *National Renewable Energy Laboratory, Golden, CO, Technical Report No. NREL/TP-500-38060,* 2009.

[25] "2.019 Design of Ocean System_Lecture 9," in *Ocean Wave Environment*, ed, 2011.

[26] J. Jonkman, A. Robertson, and G. Hayman, "HydroDyn user's guide and theory manual," *National Renewable Energy Laboratory,* 2014.

[27] J. M. Jonkman, *Definition of the Floating System for Phase IV of OC3*: Citeseer, 2010.

[28] H. M. Irvine and H. M. Irvine, *Cable structures* vol. 17: MIT press Cambridge, MA, 1981.

[29] M. Masciola, "Map++ Documentation Release 1.15," Technical report, National Renewable Energy Laboratory-NREL2016.

[30] F. G. Nielsen, T. D. Hanson, and B. r. Skaare, "Integrated dynamic analysis of floating offshore wind turbines," in *25th International Conference on Offshore Mechanics and Arctic Engineering*, 2006, pp. 671-679.
[31] B. Skaare, T. D. Hanson, F. G. Nielsen, R. Yttervik, A. M. Hansen, K. Thomsen*, et al.*, "Integrated dynamic analysis of floating offshore wind turbines," in *European Wind Energy Conference, Milan, Italy*, 2007, pp. 7-10.
[32] S. Guntur, J. M. Jonkman, B. Jonkman, Q. Wang, M. A. Sprague, M. Hind*, et al.*, "FAST v8 verification and validation for a MW-scale wind turbine with aeroelastically tailored blades," in *34th wind energy symposium*, 2016, p. 1008.
[33] A. J. Goupee, R. W. Kimball, and H. J. Dagher, "Experimental observations of active blade pitch and generator control influence on floating wind turbine response," *Renewable Energy,* vol. 104, pp. 9-19, 2017.
[34] M. Hall, A. Goupee, and J. Jonkman, "Development of performance specifications for hybrid modeling of floating wind turbines in wave basin tests," *Journal of Ocean Engineering and Marine Energy,* vol. 4, pp. 1-23, 2018.

List of figures

List of tables

List of equations